



Deposited via The University of Sheffield.

White Rose Research Online URL for this paper:

<https://eprints.whiterose.ac.uk/id/eprint/160430/>

Version: Accepted Version

Article:

Colman, M.A., Holmes, M., Whittaker, D.G. et al. (2021) Multi-scale approaches for the simulation of cardiac electrophysiology: I – sub-cellular and stochastic calcium dynamics from cell to organ. *Methods*, 185. pp. 49-59. ISSN: 1046-2023

<https://doi.org/10.1016/j.ymeth.2020.02.011>

Article available under the terms of the CC-BY-NC-ND licence
(<https://creativecommons.org/licenses/by-nc-nd/4.0/>).

Reuse

This article is distributed under the terms of the Creative Commons Attribution-NonCommercial-NoDerivs (CC BY-NC-ND) licence. This licence only allows you to download this work and share it with others as long as you credit the authors, but you can't change the article in any way or use it commercially. More information and the full terms of the licence here: <https://creativecommons.org/licenses/>

Takedown

If you consider content in White Rose Research Online to be in breach of UK law, please notify us by emailing eprints@whiterose.ac.uk including the URL of the record and the reason for the withdrawal request.

Multi-scale approaches for the simulation of cardiac electrophysiology: I - sub-cellular and stochastic calcium dynamics from cell to organ

Michael A. Colman^{a,*}, Maxx Holmes^a, Dominic G. Whittaker^{a,b}, Izzy Jayasinghe^a, Alan P. Benson^a

^aSchool of Biomedical Sciences University of Leeds, Leeds LS2 9JT, UK

^bSchool of Mathematical Sciences, University of Nottingham, Nottingham NG7 2RD, UK

*Correspondence to m.a.colman@leeds.ac.uk (MAC)

Highlights

- Computational models of cardiac calcium handling are powerful tools to understand the complex mechanisms underlying physiological and pathophysiological phenomena.
- This article describes the fundamental equations describing calcium handling at the spatial, sub-cellular scale.
- And outlines two different discretisation approaches for practical simulation of spatio-temporal sub-cellular calcium dynamics.
- Finally, multi-scale integration methods for tissue-scale simulation of stochastic dynamics are described.

Abstract

Computational models of the heart at multiple spatial scales, from sub-cellular nanodomains to the whole-organ, are a powerful tool for the simulation of cardiac electrophysiology. Application of these models has provided remarkable insight into the normal and pathological functioning of the heart. In these two articles, we present methods for modelling cardiac electrophysiology at all of these spatial scales. In part one, presented here, we discuss methods and approaches for modelling sub-cellular calcium dynamics at the whole-cell and organ scales, valuable for modelling excitation-contraction coupling and mechanisms of arrhythmia triggers.

Keywords: calcium handling, excitation-contraction coupling, spontaneous activity, cardiac tissue, electrophysiology, action potential, propagation, computational modelling

1. Intro

The periodic cycling of calcium (Ca^{2+}) ions controls excitation-contraction coupling (ECC) in cardiomyocytes, the mechanism by which electrical excitation triggers the development of mechanical force [1]. Intracellular Ca^{2+} homeostasis is relevant for maintaining appropriate cardiac performance required to meet the dynamic demands of the body, and has also been linked to pro-arrhythmogenic cellular phenomena [2,3]. Elucidation of the complex and multi-scale interactions which determine the mechanisms by which intracellular Ca^{2+} cycling underlies (patho)physiological function is therefore critical not only for fundamental

1 understanding of the electro-mechanical system of the heart, but also to the clinical motivations
2 of treating and managing life-altering and -threatening cardiovascular disease [4,5].

3 The system maintaining Ca^{2+} homeostasis comprises multiple membrane transport channels
4 and sub-cellular structures, the complex interactions of which are challenging to dissect with
5 purely experimental approaches. Computational modelling has proved a powerful tool to
6 supplement experimental studies and tease apart the mechanisms of cardiac function in health
7 and disease [6,7]. However, developing accurate and realistic models of intracellular Ca^{2+}
8 homeostasis presents a number of additional challenges compared to the point-source cell
9 models traditionally used. Namely, one must attempt to simultaneously account for: (i) the co-
10 localisation between channels at the nanometre scale; (ii) stochastic state transitions in
11 restricted nanodomains; (iii) the spatial distribution of channels and membrane structures
12 throughout the intracellular volume; and (iv) the interactions of heterogeneous cells in the
13 syncytium of cardiac tissue. Over the last decade, multiple research groups have made
14 significant advancements in the development of methodologies and approaches to address
15 these challenges [8–20]; within this context, this article focuses on those developed by and
16 utilised within our lab.

17 We will first discuss the primary components of the intracellular Ca^{2+} handling system and
18 mechanisms of pro-arrhythmogenic phenomena to provide a context for the computational
19 models. The methods described are focussed on two motivations: (i) modelling cellular spatial
20 structure-function relationships underlying ECC and dysfunctional homeostasis, and (ii) multi-
21 scale approaches for efficient modelling of Ca^{2+} -dependent spontaneous excitations in tissue.
22 The computational models referred to are provided open-source and can be found in the lab's
23 Github repository (<https://github.com/michaelcolman/>) and through the lab's website
24 (<http://physicsoftheheart.com/>). This is part one of a two-part article; see Benson et al. in this
25 issue for part two, which discusses methods for modelling structure-function relationships in
26 cardiac tissues.

27 2. The intracellular Ca^{2+} handling system

28 At the whole-cell scale, Ca^{2+} homeostasis is regulated by the balance of multiple Ca^{2+} fluxes
29 and depends on the process of Ca^{2+} -induced- Ca^{2+} -release (CICR; Figure 1A): During cellular
30 excitation, the L-type- Ca^{2+} -channels (LTCCs) open and permit an influx of Ca^{2+} from the
31 extracellular space; the elevated intracellular Ca^{2+} concentration promotes binding with the
32 type-2 ryanodine receptors (RyRs), which release a larger amount of Ca^{2+} from the intracellular
33 Ca^{2+} store (the sarcoplasmic reticulum; SR) into the bulk intracellular space. Homeostasis is
34 maintained by effluxes through the membrane channels of the sodium-calcium exchanger
35 (NCX) and the Ca^{2+} ATPase pump, which remove Ca^{2+} into the extracellular space, and the
36 SR- Ca^{2+} -pump (SERCA), which refills the SR.

37 The distributed spatial structure of the sarcolemmal and SR membranes and their associated
38 channel proteins facilitates uniform cellular contraction, but also has potentially pro-
39 arrhythmogenic implications. CICR occurs in restricted nanodomains called dyads, which co-
40 localise the LTCCs and RyRs; each dyad contains only a few LTCC and RyR channels
41 (typically 5-15 and 5-200, respectively [21]) within a very small volume ($O(10^{-3}) \mu\text{m}^3$) where
42 random state transitions can have important implications. Dyads are distributed throughout the
43 intracellular volume and are functionally coupled by Ca^{2+} diffusion, supporting robust whole-
44 cell triggered Ca^{2+} release which, in normal conditions, can normalise the stochastically-driven
45 variability of triggered Ca^{2+} sparks occurring in individual dyads. However, this functional
46 coupling in combination with inter-dyad heterogeneity has been shown to be a critical factor
47 underlying the dynamics of Ca^{2+} -transient alternans [8,22], referring to beat-to-beat
48 alternations to the magnitude of the Ca^{2+} transient and developed force which can both directly

1 impact cardiac output as well as lead to arrhythmia. Moreover, random openings of single or
 2 few RyRs can raise the local Ca^{2+} concentration sufficiently to trigger further openings within
 3 the dyad, potentially leading to a whole-dyad event: the spontaneous Ca^{2+} spark. Spatial-diffuse
 4 coupling amplifies this intrinsic feedback mechanism and provides a dynamical substrate for
 5 the propagation of microscopic fluctuations to the macroscopic scale (whole-cell) as a spark-
 6 induced-spark mediated Ca^{2+} wave (Figure 1B). Activation of NCX as this wave propagates
 7 throughout the intracellular volume results in a transient inward current that can depolarise the
 8 cell membrane as a delayed-after-depolarisation (DAD) or full triggered action potentials (TA;
 9 Figure 1B), potentially triggering spontaneous focal excitations and arrhythmia in tissue. Thus,
 10 stochastic dynamics in sub-cellular Ca^{2+} handling can have implications on whole-cell and
 11 whole-organ function; accounting for these microscopic features in efficient cell models is one
 12 major challenge faced by the community.

13 The methods described in this article aim to build multi-scale modelling approaches to
 14 accurately simulate these underlying heterogeneous sub-cellular spatial-dynamics and their
 15 impact on tissue function.

16 3. Methods for modelling sub-cellular spatial Ca^{2+} dynamics

17 This section describes methods for modelling the structure-function relationships of
 18 intracellular Ca^{2+} handling at two different levels of detail, corresponding to different
 19 discretisation approaches. The first (Figure 2A), at the coarsest resolution, approximates a cell
 20 as a 3D grid of “calcium-release-units” (CRUs) [8,23] which are comprised of multiple
 21 intracellular and SR compartments, and are thus referred to herein as **compartmentalised**
 22 models. The second (Figure 2B), higher resolution approach discretises the intracellular spaces
 23 as volumes within which free diffusion occurs [9,12,20], and are thus herein referred to as **free-**
 24 **diffusion** models. The two models operate at discretisation scales of $O(10^0) \mu\text{m}^3$ and $O(10^2)$
 25 nm^3 , respectively, and present different advantages: namely, the ability to directly study
 26 structure-function relationships at the super resolution scale (free-diffusion models), and the
 27 ability to carry out high-throughput simulations suitable for statistical analysis
 28 (compartmentalised models). The fundamental schematic structure and governing equations of
 29 the models are the same, described in the next section. Instructions and worked examples for
 30 implementing both of these model types using the source-code developed in the lab is provided
 31 in the Supplementary Material S1 – Worked Examples and the extensive documentations
 32 provided with the code.

33 3.1. Fundamental model setup

34 Whereas some of the fine details may differ, the fundamental structure of whole-cell spatio-
 35 temporal models of intracellular Ca^{2+} handling in the literature in-general comprises five
 36 compartments (Figure 2Aiii, Biii): the intracellular space is split into the compartments of the
 37 dyadic cleft, the local sub-space, and the bulk intracellular space; the SR is split into the
 38 network and junctional compartments (nSR and jSR, respectively). The dyadic cleft can be
 39 treated as a single compartment with volume v_{ds} and associated numbers of LTCCs and RyRs
 40 (these parameters can vary between individual dyads); the bulk intracellular space, network SR
 41 space and (optionally) the sub-space can be spatially coupled to their neighbours, whereas the
 42 junctional SR and dyad compartments are spatially isolated. Ca^{2+} dynamics in each of these
 43 five compartments is described by the general homeostatic equations:

$$44 \quad \frac{d[\text{Ca}^{2+}]_{cyto}}{dt} = \beta_{cyto} \left(\mathbf{D}\nabla^2[\text{Ca}^{2+}]_{cyto} + \phi_{cyto} + \left(v_{ss}/v_{cyto} \right) J_{ss} \right) \quad (1)$$

$$1 \quad \frac{d[Ca^{2+}]_{SS}}{dt} = \beta_{SS} \left(\mathbf{D}\nabla^2[Ca^{2+}]_{SS} + \phi_{SS} - J_{ss} + \left(v_{ds}/v_{ss} \right) J_{ds} \right) \quad (2)$$

$$2 \quad \frac{d[Ca^{2+}]_{nSR}}{dt} = \beta_{nSR} \left(\mathbf{D}\nabla^2[Ca^{2+}]_{nSR} + \phi_{nSR} - \left(v_{jsr}/v_{nsr} \right) J_{jsr} \right) \quad (3)$$

$$3 \quad \frac{d[Ca^{2+}]_{ds}}{dt} = \phi_{ds} - J_{ds} \quad (4)$$

$$4 \quad \frac{d[Ca^{2+}]_{jsr}}{dt} = \beta_{jsr} \left(\phi_{jsr} + J_{jsr} \right) \quad (5)$$

5 Where transfer between compartments is given by:

$$6 \quad J_{ss} = \left([Ca^{2+}]_{SS} - [Ca^{2+}]_{cyto} \right) \tau_{ss}^{-1} \quad (6)$$

$$7 \quad J_{ds} = \left([Ca^{2+}]_{ds} - [Ca^{2+}]_{SS} \right) \tau_{ds}^{-1} \quad (7)$$

$$8 \quad J_{jsr} = \left([Ca^{2+}]_{nSR} - [Ca^{2+}]_{jsr} \right) \tau_{jsr}^{-1} \quad (8)$$

9 And the general form for reaction terms are:

$$10 \quad \phi_{cyto} = J_{NaCa} + J_{pCa} + J_{Cab} - \left(J_{up} - J_{leak} \right) - J_{trpn} \quad (9)$$

$$11 \quad \phi_{nSR} = \left(J_{up} - J_{leak} \right) \left(v_i/v_{nsr} \right) \quad (10)$$

$$12 \quad \phi_{ss} = J_{NaCa_{SS}} + J_{pCa_{SS}} + J_{Cab_{SS}} \quad (11)$$

$$13 \quad \phi_{ds} = J_{rel} + J_{CaL} \quad (12)$$

$$14 \quad \phi_{jsr} = -J_{rel} \left(v_{ds}/v_{jsr} \right) \quad (13)$$

15 Where ∇^2 is the spatial Laplacian operator in 3D, β refers to instantaneous buffering, v refers
 16 to the volumes of the compartments and τ to the time-constants of diffusion. Full equations
 17 and parameters are given in the Supplementary Material S2 – Model description, and in
 18 associated publications [11–13].

19 3.2. Discretisation scheme: compartmentalised models

20 Following the approach outlined in [8,10,23], a coarse-grained and efficient discretisation of
 21 the whole-cell can be attained by considering the volumes of each compartment associated with
 22 each dyad as a single CRU (Figure 2A), corresponding to discretisation in the range 1-2 μ m.
 23 Such models assume homogeneous distances between dyads (transverse-longitudinal
 24 anisotropy can still be included) but have proved valuable in mechanistic investigation of Ca^{2+} -
 25 diffusion dependent phenomena. Each CRU contains a single volume for each of the five
 26 compartments and contains a flux from each reaction term. Spatial coupling for the cytoplasm,

1 sub-space and network SR can be approximated by coupling the relevant compartment of each
 2 CRU to its six nearest neighbours in each of the principal directions and defining a time-
 3 constant of diffusion between them; time-constants can differ between types of compartment,
 4 and in the transverse and longitudinal directions to introduce anisotropy. Thus, the diffusion
 5 terms in equations 1-3 can be approximated with the following discretisation:

$$6 \quad \mathbf{D}\nabla^2[Ca^{2+}]_{x=cyto,SS,nSR} \approx J_{Ca_diff_x} = \sum_{i=1}^{i=3} \left(\frac{e_i^{+1}[Ca^{2+}]_x + e_i^{-1}[Ca^{2+}]_x - 2e_i[Ca^{2+}]_x}{\tau_{x,e_i}} \right) \quad (14)$$

7 Where example [11,13] values for the time constants, relative to the longitudinal axis of the
 8 cell, are 2.9_{\parallel} and 2.3_{\perp} ms (cytoplasm), 12_{\parallel} and 7_{\perp} ms (network SR), and 2.2_{\parallel} and 1.35_{\perp} ms
 9 (sub-space). Every other equation is discretised by solving it locally for each CRU, n ($= 1, 2$
 10 $\dots N_{CRUs}$). Different cellular geometries can be specified by defining different extents of the
 11 CRU grid in each direction, representing, for example a typical ventricular cell ($15 \times 20 \times 65$
 12 $\approx 15 \times 20 \times 100 \mu m^3$) or with adjusted parameters to reproduce variability, remodelling or
 13 similar. Note that distances in this type of model are not explicitly defined, but are rather
 14 captured in the time constants of diffusion. Please see [8] for estimating time-constants based
 15 on distance and local buffering. These models are available in the “**Multi-scale cardiac**
 16 **simulation framework (MSCSF)**” repository on the lab’s Github.

17 3.3. Discretisation scheme: free-diffusion models

18 Following the earlier works of Li et al. 2010 [9] and Nivala et al. 2012 [20], an approach was
 19 developed in Colman et al. 2017 [12] to integrate multiple reconstructed cellular structures into
 20 free-diffusion models of spatio-temporal calcium handling (Figure 2B). Fundamental model
 21 setup is similar to those studies, with the addition of mapping functions to describe the
 22 heterogeneous structures of the SR and T-system. This approach discretises the space
 23 explicitly, rather than through compartmentalisation of CRUs. An idealised model is first
 24 created by selecting a volume to correspond to the intracellular space – either a cuboid or a
 25 cylinder with dimensions that match those of cardiac cells ($10\text{-}20 \mu m \times 10\text{-}20 \mu m \times 50\text{-}150$
 26 μm). This volume can be discretised at a chosen resolution in the range $\Delta x = 100 - 250$ nm and
 27 the diffusion terms in equations 1-3 are modelled by the isotropic, 6-node finite difference
 28 approximation:

$$29 \quad \mathbf{D}\nabla^2[Ca^{2+}]_{x=cyto,SS,nSR} \approx \sum_{i=1}^{i=3} \mathbf{D} \left(\frac{e_i^{+1}[Ca^{2+}]_x + e_i^{-1}[Ca^{2+}]_x - 2e_i[Ca^{2+}]_x}{\Delta x_{e_i}^2} \right) \quad (15)$$

30 3.3.1. Model setup

31 The model can be considered to be tri-domain, wherein each voxel of the intracellular space
 32 comprises domains corresponding to the bulk intracellular space, the network SR space, and
 33 the sub-space (Figure 2B). Individual voxels can be selected to correspond to the locations of
 34 the dyads, and therefore also contain a dyad and junctional SR compartment (which are coupled
 35 to the sub-space and network SR compartments of that voxel, respectively). Mapping functions
 36 must therefore be created to relate dyad m ($m = 1, 2 \dots M$) with voxel n ($n = 1, 2 \dots N$), where
 37 M and N are the total numbers of dyads and voxels in the model, respectively. These functions
 38 are defined as $\theta_{dyad}(m) = n$ and inverse function $\theta_{dyad}^{-1}(n) = m$. Following this discretisation,
 39 the model equations must be updated to give:

$$1 \quad {}^n J_{ds} = \left(\begin{array}{c} \theta_{dyad}^{-1}(n)=m [Ca^{2+}]_{ds} - {}^n [Ca^{2+}]_{SS} \\ 0 \end{array} \right) \tau_{ds}^{-1} \left. \begin{array}{l} \forall n \in \theta_{dyad}(m) \\ \forall n \notin \theta_{dyad}(m) \end{array} \right\} \quad (16)$$

$$2 \quad {}^n J_{jSR} = \left(\begin{array}{c} \theta_{dyad}^{-1}(n)=m [Ca^{2+}]_{nSR} - [Ca^{2+}]_{jSR} \\ 0 \end{array} \right) \tau_{jSR}^{-1} \left. \begin{array}{l} \forall n \in \theta_{dyad}(m) \\ \forall n \notin \theta_{dyad}(m) \end{array} \right\} \quad (17)$$

3 Where all dyad-specific dynamics ($[Ca^{2+}]_{ds}$ and $[Ca^{2+}]_{jSR}$ terms) are solved only for voxels
4 containing dyads (note that the above ensures those which do not contain dyads have no
5 contribution from them). In the fully idealised models, these dyads can be evenly distributed
6 throughout the cell volume at intervals of 1-2 μm (Figure 2Bii), or according to randomly
7 produced distributions for theoretical study; the distances between dyads is necessarily limited
8 to the same discretisation as the chosen space step, Δx .

9 3.3.2. Distributing membrane and SR fluxes

10 In fully idealised approaches, the sarcolemmal membrane (surface and TT) and SR occupy the
11 entire intracellular volume and are present in every voxel. However, this is not physiologically
12 representative nor a requirement of this approach: both may be restricted to a subset of the
13 intracellular voxels and thus have their own structure. The structures themselves can be derived
14 from experimental imaging data, as described later, or theoretically generated ‘‘cartoon’’
15 geometries. Dependent on the available data and desires, some or all of the following
16 considerations can be included: (i) non-idealised dyad distribution and heterogeneous RyR and
17 LTCC channel numbers; (ii) structure of the surface sarcolemma and T-system; (iii) structure
18 of the SR; (iv) relative expression of sarcolemmal and/or SR channels along these membranes.

19 Distributing dyads according to different spatial geometries involves defining the mapping
20 functions to correctly relate dyads to voxels. Similar mapping functions can also be used to
21 localise and distribute the membrane and SR fluxes according to the desired structure. Thus,
22 we introduce the membrane maps ($\theta_{mem}(p) = n$; $\theta_{mem}^{-1}(n) = p$) and SR maps ($\theta_{SR}(q) = n$; $\theta_{SR}^{-1}(n) = q$)
23 which relate membrane and SR voxels ($p = 1, 2 \dots P$; $q = 1, 2 \dots Q$) to the intracellular
24 space voxel. Note that under these additions, the model is no-longer a homogeneous tri-domain
25 model, as not every voxel necessarily contains a network SR domain. Thus, the reaction term
26 for the cytoplasm (equation 9) and SR (equation 10) are updated accordingly:

$$27 \quad {}^n \phi_i = \left. \begin{array}{l} - {}^n J_{trpn} \\ \theta_{mem}^{-1}(n)=p J_{NaCa} + {}^p J_{pCa} + {}^p J_{Cab} - {}^n J_{trpn} \\ - \left(\theta_{SR}^{-1}(n)=q J_{up} - {}^q J_{leak} \right) - {}^n J_{trpn} \\ \theta_{mem}^{-1}(n)=p J_{NaCa} + {}^p J_{pCa} + {}^p J_{Cab} - \left(\theta_{SR}^{-1}(n)=q J_{up} - {}^q J_{leak} \right) - {}^n J_{trpn} \end{array} \right\} \left. \begin{array}{l} \forall n \notin \theta_{mem}(p) \wedge \notin \theta_{SR}(q) \\ \forall n \in \theta_{mem}(p) \wedge \notin \theta_{SR}(q) \\ \forall n \notin \theta_{mem}(p) \wedge \in \theta_{SR}(q) \\ \forall n \in \theta_{mem}(p) \wedge \in \theta_{SR}(q) \end{array} \right\} \quad (18)$$

$$29 \quad \theta_{SR}^{-1}(n)=q \phi_{nSR} = \left(\begin{array}{c} ({}^q J_{up} - {}^q J_{leak})(v_i/v_{nsr}) \\ 0 \end{array} \right) \left. \begin{array}{l} \forall n \in \theta_{SR}(q) \\ \forall n \notin \theta_{SR}(q) \end{array} \right\} \quad (19)$$

1 Where ${}^qJ_{up}, {}^qJ_{leak} = f(\theta^{SR(q)=n}[Ca^{2+}]_{cyto}, {}^q[Ca^{2+}]_{SR})$. For any structures considered idealised
 2 (occupying the entire intracellular volume) there is therefore a one-to-one mapping with the
 3 intracellular space, and the general form of the equation is restored.

4 3.4. Heterogeneous ion channel expression in the sub-cellular volume

5 Heterogeneous expression of the flux channels can be incorporated by scaling the local
 6 maximal flux rates and/or channel numbers around the mean while maintaining total channel
 7 expression. For the membrane fluxes this gives:

$$8 \quad \begin{aligned} & {}^pJ_X = {}^pG_X \cdot J_X^{\max} \cdot f(\theta_{mem}^{(p)=n}[Ca^{2+}]_{cyto}, V_m) \\ & \sum_{p=1}^{p=P} \left(\frac{{}^pG_X}{P} \right) = 1 \end{aligned} \quad (20)$$

9 Where X represents any of the membrane fluxes in equation 9. Similarly, for the SR fluxes (J_{up}
 10 and J_{leak}):

$$11 \quad \begin{aligned} & {}^qJ_X = {}^qG_X \cdot J_X^{\max} \cdot f(\theta_{sr}^{(q)=n}[Ca^{2+}]_{cyto}, {}^q[Ca^{2+}]_{SR}) \\ & \sum_{q=1}^{q=Q} \left(\frac{{}^qG_X}{Q} \right) = 1 \end{aligned} \quad (21)$$

12 This approach can be equally applied to both compartmentalised and free-diffusion models.

13 4. Image-based modelling approaches

14 This section outlines approaches for modelling controllable and experimentally-matched
 15 heterogeneous structures in both types of spatial cell model. These approaches can be applied
 16 in future studies to help to rigorously establish the link between structure and emergent function
 17 in both physiological and pathophysiological conditions.

18 4.1. Direct image-based modelling using the free-diffusion models

19 The free-diffusion model developed in Colman et al. 2017 [12] and described above was
 20 specifically designed for the ability to directly include experimental reconstructions of the sub-
 21 cellular membrane structures and channel distribution, permitting *in silico* functional
 22 assessment of specific cellular structure. This section outlines the approaches for processing
 23 and discretising high-resolution cellular structural data for simulations; the reader is referred
 24 to the original paper for further details. The experimental imaging approaches to acquire these
 25 structural data are described elsewhere [24–26].

26 The model setup already includes the functionality for the sarcolemmal and SR membranes to
 27 contain their own structure within the intracellular volume. Thus, all that is required is to create
 28 the mapping functions which relate the dyad, membrane and SR voxels to intracellular voxels.
 29 The first step is to segment the desired structures from the imaging data (Figure 3A) based on
 30 user-determined thresholds – the desired output is binary: 1 representing the presence of the
 31 structure, 0 representing its absence.

32 The dyads in the model should be point-sources occupying one voxel each, and so down-
 33 sampling imaging data to the model discretisation should be relatively simple (Figure 3B). The
 34 T-tubules and SR should be continuously connected networks; smoothing of the data may be
 35 required to achieve this. For the T-tubules, the structure may be crudely down-sampled either
 36 using an image-processing tool, or using an explicitly defined threshold for the number of high-
 37 resolution voxels which correspond to its presence at low resolution. The process is more

1 complex for the SR, as the down-sampled resolutions may significantly obscure the network
2 structure of the system (Figure 3C). Thus, rather than simple down-sampling, the network is
3 first skeletonised and the connections along the network are mapped. The skeleton can then be
4 down-sampled, with the connection map imposed to ensure new connections are not created
5 through this down-sampling (Figure 3D).

6 Once we have structures which represent the T-system and SR at the spatial resolution of the
7 model's intracellular space, sequentially numbering each element of the geometries allows a
8 simple mapping of voxel n to structure map p, q . The fluxes interacting with the cytoplasm are
9 thusly localised to these structures; diffusion of Ca^{2+} in the SR is solved using the connection
10 map as a pseudo-1D cable.

11 If data on channel expression along the membranes are available, then the local flux at each
12 map element can be scaled according to this relative expression data. The relative expression
13 should be normalised to meet the constraint that the average is 1 (i.e. whole-cell channel
14 expression is unaffected) and then this relative expression map defines local $^{p,q}G_x$ in equations
15 20-21.

16 4.2. Image-based modelling using the compartmentalised models

17 Despite the clear value of the structurally detailed free-diffusion models for investigations of
18 heterogeneous sub-cellular structure, they are computationally intensive and restricted to the
19 structural data available or cartoon geometries. The compartmentalised models can also be
20 used for structurally heterogeneous investigation in a more systematic and general approach.
21 The range of heterogeneities investigated is more limited than the free-diffusion model (for
22 example, inter-dyad distance and co-localisation distances are fixed in the current setup of the
23 model), but can include: numbers of RyRs/LTCCs in each dyad, and the respective dyad and
24 jSR volumes; the relative expression of all other Ca^{2+} -flux carrying channels in each CRU.
25 These heterogeneities can be included by producing 3D maps which scale flux strength (or any
26 other) parameters in individual CRUs relative to the global value, e.g. by directly setting the
27 local flux scale-factor $^{p,q}G_x$. This section will first discuss methods for producing spatially
28 correlated relative expression maps, followed by methods for analysing real imaging data to
29 perform image-based modelling using these idealised models.

30 4.2.1. Modelling spatially heterogeneous channel expression

31 A crude approach to modelling sub-cellular heterogeneity in channel expression could be
32 simply to use a random number generator to produce a randomly populated scaling map,
33 imposing a selected probability density function. However, a spatial random field can also be
34 used which accounts for the spatial correlation in channel expression, ensuring the expression
35 in one CRU is not independent of that in its neighbour. A random field, $F(x)$, is a random
36 function over some arbitrary (usually multi-dimensional) system, which can be described as a
37 set of continuous indexed variables $x \in \Omega$, where Ω is an open set of \mathbb{R}^d which describe the
38 geometry of the system [27,28]. The main statistics of random fields are the mean, variance
39 and correlation length (length scale), which can have their own functions.

40 One class of correlated random field is a Gaussian random field (GRF) which uses the Gaussian
41 probability density function with an exponential covariance (a 1-D GRF is also called a
42 Gaussian Process) [29]. Through applying Gaussian functions to these statistics, the random
43 field can be constrained, allowing 3D heterogeneous expression maps (Figure 4A) to be
44 produced with given spatial parameters. The length-scale, λ , determines the spatial extent of
45 correlated expression: at the CRU resolution (i.e. $1\mu\text{m}$) this is equivalent to a spatially
46 uncorrelated map; as length scale increases, the rate of spatial variation decreases (Figure 4B).
47 Anisotropic maps can also be produced wherein the length scales in the transverse and
48 longitudinal directions are not equal (i.e. $\lambda_T \neq \lambda_L$; Figure 4B), which may be more

1 representative of cardiac sub-cellular structure. It is vital to impose the constraint when
2 producing these maps that the mean scale factor remains 1, such that the inclusion of such
3 heterogeneity does not affect whole-cell expression.

4 The impact of such sub-cellular heterogeneity on the spatial and average properties of the Ca^{2+}
5 transient can be substantial, in particular when heterogeneity in multiple targets (e.g. SERCA
6 and RyR) are considered in combination (Figure 4C). Preliminary simulations indicate such
7 heterogeneities may be linked to both Ca^{2+} -transient alternans and spontaneous excitation. For
8 those interested in exploring this further, we have developed user-friendly tools to generate
9 these maps, suitable for use in our simulation framework, which can be found in the
10 “Sub_cellular_heterogeneity_TOOLKIT” repository on the lab’s Github.

11 4.2.2. Methods for data processing for image-based modelling

12 This section discusses processing cellular imaging datasets in order to extract the information
13 necessary to generate spatial maps which are congruent with the experimentally measured
14 properties. In brief, we want to extract the length scales in the transverse and longitudinal
15 directions which may be used as inputs to generate sets of randomly produced maps with those
16 properties. A variogram model is used to estimate these length scales from the microscopy
17 data.

18 Extracting the variation parameters from microscopy data required the construction of a semi-
19 automatic pipeline which processes the image data into a suitable format for analysis, and a
20 method of fitting the processed data to some spatial covariance function which includes a
21 description of correlation length scales. This semi-automatic pipeline is available in the
22 “Sub_cellular_heterogeneity_TOOLKIT” repository on the lab’s Github, which contains
23 worked examples for data processing. The process of this analysis is described below.

24 The processed dataset must contain a suitably large quantity of data in order to obtain
25 meaningful values of longitudinal and transversal length scales. The image data should be
26 rotated such that the longitudinal and transversal axes are in alignment with the x and y axes
27 of the image (Figure 5A). Rotated images are then cropped and down-sampled to a resolution
28 of 1-2 μm (Figure 5A). This down-sampling is essential for length-scale analysis, as we require
29 a continuous distribution representing the average relative expression of each channel per
30 CRU, suitable for comparing different CRUs, and therefore need to remove the internal
31 underlying membrane structure; the down-sampled image should be suitable for visualisation
32 as a contour map (Figure 5A). The variogram fitting procedure can then be applied to obtain
33 the relevant parameters corresponding to that slice (Figure 5A). The process is repeated for all
34 suitable x-y slices in the z-stack of images, and the summary parameters for the whole-cell can
35 be obtained. These parameters can then be used to generate sets of 3D heterogeneity maps for
36 use in simulations (Figure 5B).

37 5. Methods for multi-scale investigation of spontaneous calcium 38 release

39 Multi-scale investigation of spontaneous Ca^{2+} release events (SCRE) is one of the major
40 motivations for developing such detailed models of spatio-temporal Ca^{2+} handling. The
41 challenge is that the spatial models discussed above are unsuitable for tissue-scale simulations,
42 whereas efficient point-source cell models cannot reproduce stochastically induced SCRE. In
43 parallel with the pioneering work of [18,19,30,31], an independent novel approach was
44 developed to accurately reproduce the statistics and dynamics of SCRE in efficient cell models
45 suitable for tissue simulations [11,13,32]. Described in detail in Colman 2019 [13], this
46 involved the introduction of spontaneous release functions (SRF): analytical waveforms
47 describing RyR open state occupancy with controllable parameters to match the timing,

1 amplitude and duration of SCORE observed in the spatial cell models and/or experiments. These
 2 functions, and algorithms to implement them with dynamic cell models, are packaged with the
 3 MSCSF on the lab's Github.

4 5.1. The Spontaneous Release Functions

5 The SRF aim to capture the temporal evolution of the open RyR waveform associated with
 6 SCORE, based on simulated SCORE emerging from the compartmentalised 3D cell model (Figure
 7 6A). Waveforms occur in broadly two forms: long-duration, spike-and-plateau like (e.g. at low
 8 Ca^{2+} load), and short-duration spike-like (e.g. at high Ca^{2+} load; Figure 6A). The primary
 9 properties of these waveforms which need to be reproduced are: (1) the initiation time, t_i ,
 10 referring to the time of onset of SCORE; (2) the duration of the waveform; and (3) the amplitude.
 11 These parameters can be used to define SRF which approximate this temporal evolution:

$$12 \quad N_{RyR_O} = N_{RyR_O}^{peak} \left[\left(1 + e^{-(t-t_i)/k_1} \right) \left(1 + e^{-(t-t_2)/k_2} \right) \right]^{-1} \quad (22)$$

$$13 \quad t_1 = t_i + 0.5(t_p - t_i) \quad (23)$$

$$14 \quad t_2 = t_p + 0.5(t_f - t_p) \quad (24)$$

$$15 \quad k_1 = 0.1689(t_p - t_i) + 0.00255 \quad (25)$$

$$16 \quad k_2 = 0.1689(t_f - t_p) + 0.00255 \quad (26)$$

17 where t_i is the initiation time of the SCORE, t_f is the end time (duration, λ , thus = $t_f - t_i$), t_p is the
 18 time of the peak of the waveform and $N_{RyR_O}^{peak}$ is the peak of open proportion RyR (Figure
 19 3D). The constants in equations (25,26) were obtained from best fits to the waveforms
 20 observed. The function for the plateau-like waveform (corresponding to durations longer than
 21 300 ms) is derived from the same parameters:

$$22 \quad N_{RyR_O} = N_{RyR_O}^{plateau} \left[\left(1 + e^{-(t-(t_i+17.5))/5.946} \right) \left(1 + e^{-(t-(t_f-17.5))/5.946} \right) \right]^{-1} + \quad (27)$$

$$\left(N_{RyR_O}^{peak} - N_{RyR_O}^{plateau} \right) \left[\left(1 + e^{-(t-(t_p-25))/5.946} \right) \left(1 + e^{-(t-(t_p+17.5))/5.946} \right) \right]^{-1}$$

23 Where $N_{RyR_O}^{plateau}$ is the amplitude of the plateau.

24 Due to the stochastic nature of SCORE, these properties are all variable and described by
 25 distributions (Figure 6B). In order to appropriately determine individual waveform parameters,
 26 these can be randomly sampled from the defined distributions.

27 (1) - t_i : The probability density functions for the initiation time do not demonstrate a normal
 28 distribution, but rather a skewed distribution. The cumulative frequency is well approximated
 29 by the use of two simple sigmoidal functions (Figure 6B):

$$30 \quad F(t_i) = \left. \begin{aligned} F_1(t_i) &= \left(2CF_{t_i, Sep} \right) \left(1 + e^{-(t_i - t_{i, sep})/k_{r1}} \right)^{-1} \\ F_2(t_i) &= \left(2(1 - CF_{t_i, Sep}) \right) \left(1 + e^{-(t_i - t_{i, sep})/k_{r2}} \right)^{-1} - 1 + 2CF_{t_i, Sep} \end{aligned} \right\} \begin{aligned} &t_i < t_{i, Sep} \\ &t_i \geq t_{i, Sep} \end{aligned} \quad (28)$$

1 The distribution for t_i is therefore determined by four parameters: the initiation time
 2 corresponding to the point where the functions are separated ($t_{i,sep}$); the cumulative frequency
 3 at this point ($CF_{t_i,sep} = F(t_i)|_{t_i=t_{i,sep}}$), and the gradient parameter of each function (k_{F1} , k_{F2} -
 4 corresponding to the width of the distribution either side of $t_{i,sep}$).

5 (2) – λ : The distributions for the duration are also non-normal, and well approximated by two
 6 sigmoidal functions describing the cumulative frequency for half of the data either side of the
 7 median duration (MD):

$$8 \quad F(MD) = \left. \begin{aligned} F_{D1}(MD) &= \left(1 + e^{-(\lambda - MD)/0.261DW_1}\right)^{-1} \\ F_{D2}(MD) &= \left(1 + e^{-(\lambda - MD)/0.261DW_2}\right)^{-1} \end{aligned} \right\} \begin{aligned} \lambda < MD \\ \lambda \geq MD \end{aligned} \quad (29)$$

9 Where the widths (DW_1 , DW_2 , in ms) are a function of the MD , given by:

$$10 \quad DW_1 = A_{DW1} \left(1 + e^{-(MD - a_{DW1})/k_{DW1}}\right)^{-1} + DW_1^{\min} \quad (30)$$

$$11 \quad DW_2 = A_{DW2} \left(1 + e^{-(MD - a_{DW2})/k_{DW2}}\right)^{-1} + DW_2^{\min} \quad (31)$$

12 The duration distribution is therefore completely described by the median, MD . Note that the
 13 widths (DW_1 , DW_2) could also be specified directly for complete control over the variability in
 14 duration. Within this, the timing of the peak, t_p , varies approximately evenly, occurring between
 15 25 ms after the initiation (t_i) and 52 ms before the final time (t_f).

16 (3) - $N_{RyR_O}^{peak}$, $N_{RyR_O}^{plateau}$: The amplitude correlates strongly with duration, λ :

$$17 \quad \langle N_{RyR_O}^{peak} \rangle = 692.99\lambda^{-1.6} + 0.059 \quad (32)$$

$$18 \quad \langle N_{RyR_O}^{plateau} \rangle = 31.09(0.01\lambda)^{-7.39} + 0.034 \quad \text{if } \lambda > 300ms \quad (33)$$

19 Full equations and parameters are presented in the Supplementary Material S2 – Model
 20 description. With this setup, therefore, all parameters of the waveform are derived from two
 21 primary waveform properties: the initiation time, t_i , and the duration, λ , which also determine
 22 the peak time and amplitude; the distributions describing the variability of these properties is
 23 entirely described by 5-7 parameters ($t_i = f(t_{i,sep}, CF_{t_i,sep}, k_{F1}, k_{F2})$; $\lambda = f(MD, DW_1, DW_2)$ where
 24 $DW_1, DW_2 = f(MD)$ or specified). Directly, these parameters can be defined by the user to
 25 investigate the impact of these distributions on cellular SCORE and its manifestation in tissue.
 26 A worked example, introducing a pathophysiological model and deriving the resulting SRF, is
 27 provided in Supplementary Material S1 – Worked Examples.

28 It is also valuable to be able to determine these distribution parameters dynamically during a
 29 simulation, based on the environmental variable of the SR - Ca^{2+} load. Specific approximations
 30 can be performed to match the behaviour of the cell models under different conditions (Figure
 31 6C). Moreover, a general and controllable approach was developed to facilitate systematic
 32 analysis in the wide parameter space: The SR dependence of these distribution parameters can
 33 be defined by functions of SR- Ca^{2+} load and user-defined parameters, offering full control of
 34 SCORE dynamics (Figure 6C):

$$35 \quad CaSR_{\min} = CaSR_{\text{threshold}} - 0.5CaSR_{p_range} \quad (34)$$

$$1 \quad P(SCR) = f_1([Ca^{2+}]_{SR}) = \left[1 + \exp\left(-([Ca^{2+}]_{SR} - CaSR_{threshold}) / 0.1CaSR_{P_range}\right) \right]^{-1} \quad (35)$$

$$2 \quad t_{i_Sep} = f_2([Ca^{2+}]_{SR}) = \left(t_{i_Sep}^{\max} - t_{i_Sep}^{\min} \right) e^{\left(-5([Ca^{2+}]_{SR} - CaSR_{\min}) / (CaSR_{\max} - CaSR_{\min}) \right)} + t_{i_Sep}^{\min} \quad (36)$$

$$3 \quad MD = f_3([Ca^{2+}]_{SR}) = \left(MD^{\max} - MD^{\min} \right) e^{\left(-5([Ca^{2+}]_{SR} - CaSR_{\min}) / (CaSR_{\max} - CaSR_{\min}) \right)} + MD^{\min} \quad (37)$$

$$4 \quad k_{F_1} = f_1(t_{i_Sep}) = 0.145 \left[\left(t_{i_width}^{\max} - t_{i_width}^{\min} \right) \left[\left(t_{i_Sep} - t_{i_Sep}^{\min} \right) / \left(t_{i_Sep}^{\max} - t_{i_Sep}^{\min} \right) \right]^{H_{width}} + t_{i_width}^{\min} \right] \quad (38)$$

$$5 \quad k_{F_2} = 1.5k_{F_1} \quad (39)$$

$$6 \quad DW_1 = f_1(MD) = \left(\lambda_{width}^{\max} - \lambda_{width}^{\min} \right) \left[\left(MD - MD^{\min} \right) / \left(MD^{\max} - MD^{\min} \right) \right]^{H_{width}} + \lambda_{width}^{\min} \quad (40)$$

$$7 \quad DW_2 = DW_1 \quad (41)$$

8 Where the user-defined parameters refer to: The threshold for SCORE ($CaSR_{threshold}$); The SR-
 9 Ca^{2+} range over which $P(SCR)$ varies from 0 to 1 ($CaSR_{P_range}$); The maximal SR- Ca^{2+} above
 10 which SCORE distributions converge ($CaSR_{max} > CaSR_{threshold} + CaSR_{P_range}$); The minimum and
 11 maximum t_{i_Sep} and MD ($t_{i_Sep}^{\min}$, $t_{i_Sep}^{\max}$, MD^{\min} , MD^{\max}); The t_i and λ distribution widths at
 12 these extremes ($t_{i_width}^{\min}$, $t_{i_width}^{\max}$, λ_{width}^{\min} , λ_{width}^{\max}); And the non-linearity of width variance
 13 (H_{width}).

14 The framework therefore uses the detailed, spatial cell models to derive the form of these SRF
 15 (Figure 6A-B); user inputs and/or SR- Ca^{2+} load are then used to define the distributions (Figure
 16 6C), from which SRF parameters are randomly sampled to define individual waves (Figure
 17 6D); these can then be integrated with non-spatial cell models, suitable for simulation in tissue
 18 (Figure 6E). This approach provides the means to investigate the mechanisms of
 19 synchronisation and dynamic interactions with tissue structure and arrhythmia conduction
 20 patterns such as re-entry [13].

21 6. Summary and conclusions

22 In this article, we have outlined methods for modelling sub-cellular spatial Ca^{2+} dynamics in
 23 cardiac cells, from the super-resolution through whole-cell up to the whole-heart scales. Such
 24 models are a powerful tool to investigate the multi-scale mechanisms underlying normal and
 25 abnormal cellular ECC as well as the emergence of Ca^{2+} -dependent arrhythmia.

26 7. Funding

27 Supported by a Medical Research Council Strategic Skills Fellowship to MC
 28 (MR/M014967/1) and a British Heart Foundation project grant to AB (PG/16/74/32374).

30 8. Supporting information

31 All of the tools discussed in this article are available from the repository
 32 (<https://github.com/michaelcolman/>).

33 Worked examples are provided in the Supplementary Material S1 – Worked Examples.

1 Full model equations are provided in the Supplementary Material S2 – Model Description.

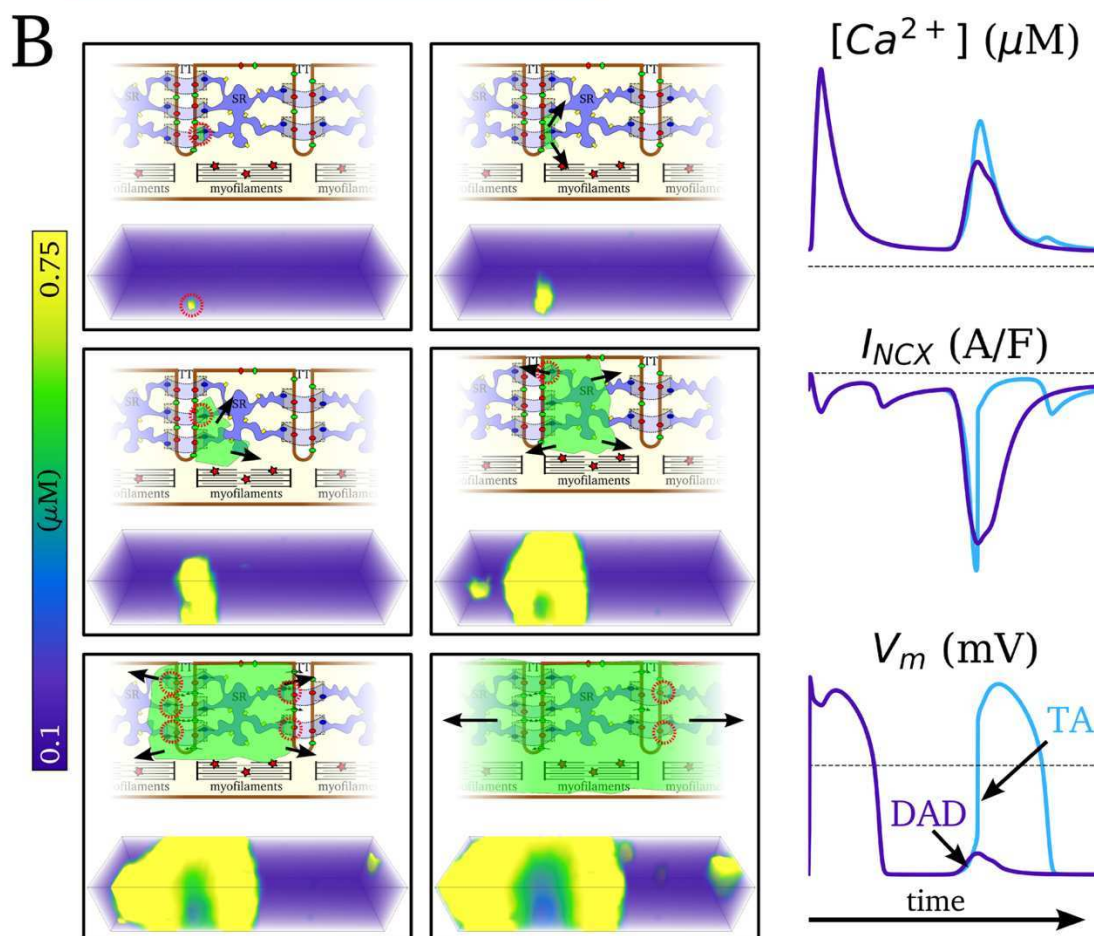
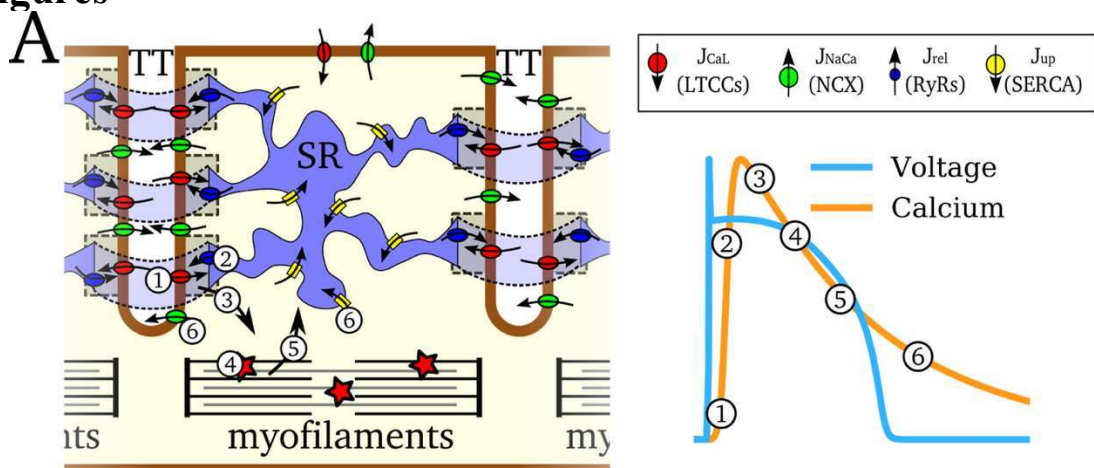
2 9. References

- 3 1. Eisner DA, Caldwell JL, Kistamás K, Trafford AW. Calcium and Excitation-Contraction
4 Coupling in the Heart. *Circ Res*. 2017 Jul 7;121(2):181–95.
- 5 2. Eisner DA, Kashimura T, Venetucci LA, Trafford AW. From the ryanodine receptor to
6 cardiac arrhythmias. *Circ J Off J Jpn Circ Soc*. 2009 Sep;73(9):1561–7.
- 7 3. Nattel S, Dobrev D. The multidimensional role of calcium in atrial fibrillation
8 pathophysiology: mechanistic insights and therapeutic opportunities. *Eur Heart J*. 2012
9 Aug;33(15):1870–7.
- 10 4. Levy D, Kenchaiah S, Larson MG, Benjamin EJ, Kupka MJ, Ho KKL, et al. Long-term
11 trends in the incidence of and survival with heart failure. *N Engl J Med*. 2002 Oct
12 31;347(18):1397–402.
- 13 5. Ceonodolea AD, Bal R, Severens JL. Epidemiology and Management of Atrial
14 Fibrillation and Stroke: Review of Data from Four European Countries. *Stroke Res Treat*.
15 2017;2017:8593207.
- 16 6. Trayanova NA, Chang KC. How computer simulations of the human heart can improve
17 anti-arrhythmia therapy. *J Physiol*. 2016;594(9):2483–502.
- 18 7. Vagos M, van Herck IGM, Sundnes J, Arevalo HJ, Edwards AG, Koivumäki JT.
19 Computational Modeling of Electrophysiology and Pharmacotherapy of Atrial
20 Fibrillation: Recent Advances and Future Challenges. *Front Physiol* [Internet]. 2018
21 [cited 2019 Jun 13];9. Available from:
22 <https://www.frontiersin.org/articles/10.3389/fphys.2018.01221/full>
- 23 8. Restrepo JG, Weiss JN, Karma A. Calsequestrin-mediated mechanism for cellular
24 calcium transient alternans. *Biophys J*. 2008 Oct;95(8):3767–89.
- 25 9. Li P, Wei W, Cai X, Soeller C, Cannell MB, Holden AV. Computational modelling of
26 the initiation and development of spontaneous intracellular Ca²⁺ waves in ventricular
27 myocytes. *Philos Transact A Math Phys Eng Sci*. 2010 Aug 28;368(1925):3953–65.
- 28 10. Song Z, Ko CY, Nivala M, Weiss JN, Qu Z. Calcium-voltage coupling in the genesis of
29 early and delayed afterdepolarizations in cardiac myocytes. *Biophys J*. 2015 Apr
30 21;108(8):1908–21.
- 31 11. Colman MA, Perez Alday EA, Holden AV, Benson AP. Trigger vs. Substrate: Multi-
32 Dimensional Modulation of QT-Prolongation Associated Arrhythmic Dynamics by a
33 hERG Channel Activator. *Front Physiol* [Internet]. 2017 [cited 2018 Nov 29];8. Available
34 from: <https://www.frontiersin.org/articles/10.3389/fphys.2017.00757/full#B21>
- 35 12. Colman MA, Pinali C, Trafford AW, Zhang H, Kitmitto A. A computational model of
36 spatio-temporal cardiac intracellular calcium handling with realistic structure and spatial
37 flux distribution from sarcoplasmic reticulum and t-tubule reconstructions. *PLoS Comput
38 Biol* [Internet]. 2017 Aug 31 [cited 2019 Mar 4];13(8). Available from:
39 <https://www.ncbi.nlm.nih.gov/pmc/articles/PMC5597258/>

- 1 13. Colman MA. Arrhythmia Mechanisms and Spontaneous Calcium Release: Bi-directional
2 Coupling Between Re-entrant and Focal Excitation. *PLOS Comput Biol.* 2019;In press.
- 3 14. Gaur N, Rudy Y. Multiscale modeling of calcium cycling in cardiac ventricular myocyte:
4 macroscopic consequences of microscopic dyadic function. *Biophys J.* 2011 Jun
5 22;100(12):2904–12.
- 6 15. Nivala M, Song Z, Weiss JN, Qu Z. T-tubule disruption promotes calcium alternans in
7 failing ventricular myocytes: mechanistic insights from computational modeling. *J Mol
8 Cell Cardiol.* 2015 Feb;79:32–41.
- 9 16. Song Z, Liu MB, Qu Z. Transverse tubular network structures in the genesis of
10 intracellular calcium alternans and triggered activity in cardiac cells. *J Mol Cell Cardiol.*
11 2018 Jan;114:288–99.
- 12 17. Vierheller J, Neubert W, Falcke M, Gilbert SH, Chamakuri N. A multiscale computational
13 model of spatially resolved calcium cycling in cardiac myocytes: from detailed cleft
14 dynamics to the whole cell concentration profiles. *Front Physiol* [Internet]. 2015 [cited
15 2019 Jul 11];6. Available from:
16 <https://www.frontiersin.org/articles/10.3389/fphys.2015.00255/full>
- 17 18. Campos FO, Shiferaw Y, Prassl AJ, Boyle PM, Vigmond EJ, Plank G. Stochastic
18 spontaneous calcium release events trigger premature ventricular complexes by
19 overcoming electrotonic load. *Cardiovasc Res.* 2015 Jul 1;107(1):175–83.
- 20 19. Campos FO, Shiferaw Y, Weber dos Santos R, Plank G, Bishop MJ. Microscopic
21 Isthmuses and Fibrosis Within the Border Zone of Infarcted Hearts Promote Calcium-
22 Mediated Ectopy and Conduction Block. *Front Phys* [Internet]. 2018 [cited 2019 Mar
23 13];6. Available from: <https://www.frontiersin.org/articles/10.3389/fphys.2018.00057/full>
- 24 20. Nivala M, de Lange E, Rovetti R, Qu Z. Computational Modeling and Numerical Methods
25 for Spatiotemporal Calcium Cycling in Ventricular Myocytes. *Front Physiol* [Internet].
26 2012 May 8 [cited 2020 Feb 10];3. Available from:
27 <https://www.ncbi.nlm.nih.gov/pmc/articles/PMC3346978/>
- 28 21. Jayasinghe I, Clowsley AH, Lin R, Lutz T, Harrison C, Green E, et al. True Molecular
29 Scale Visualization of Variable Clustering Properties of Ryanodine Receptors. *Cell Rep.*
30 2018 Jan 9;22(2):557–67.
- 31 22. Alvarez-Lacalle E, Echebarria B, Spalding J, Shiferaw Y. Calcium alternans is due to an
32 order-disorder phase transition in cardiac cells. *Phys Rev Lett.* 2015 Mar
33 13;114(10):108101.
- 34 23. Rovetti R, Cui X, Garfinkel A, Weiss JN, Qu Z. Spark-induced sparks as a mechanism of
35 intracellular calcium alternans in cardiac myocytes. *Circ Res.* 2010 May
36 28;106(10):1582–91.
- 37 24. Pinali C, Bennett H, Davenport JB, Trafford AW, Kitmitto A. Three-dimensional
38 reconstruction of cardiac sarcoplasmic reticulum reveals a continuous network linking
39 transverse-tubules: this organization is perturbed in heart failure. *Circ Res.* 2013 Nov
40 8;113(11):1219–30.

- 1 25. Jayasinghe I, Clowsley AH, Lin R, Lutz T, Harrison C, Green E, et al. True Molecular
2 Scale Visualization of Variable Clustering Properties of Ryanodine Receptors. *Cell Rep.*
3 2018 09;22(2):557–67.
- 4 26. Jayasinghe I, Clowsley AH, de Langen O, Sali SS, Crossman DJ, Soeller C. Shining New
5 Light on the Structural Determinants of Cardiac Couplon Function: Insights From Ten
6 Years of Nanoscale Microscopy. *Front Physiol* [Internet]. 2018 [cited 2019 May 11];9.
7 Available from: <https://www.frontiersin.org/articles/10.3389/fphys.2018.01472/full>
- 8 27. Arregui-Mena JD, Margetts L, Mummery PM. Practical Application of the Stochastic
9 Finite Element Method. *Arch Comput Methods Eng.* 2016 Mar;23(1):171–90.
- 10 28. Sudret B. Stochastic Finite Element Methods and Reliability A State-of-the-Art Report.
11 :189.
- 12 29. Clayton RH. Dispersion of Recovery and Vulnerability to Re-entry in a Model of Human
13 Atrial Tissue With Simulated Diffuse and Focal Patterns of Fibrosis. *Front Physiol*
14 [Internet]. 2018 [cited 2019 May 23];9. Available from:
15 <https://www.frontiersin.org/articles/10.3389/fphys.2018.01052/full>
- 16 30. Xie Y, Sato D, Garfinkel A, Qu Z, Weiss JN. So little source, so much sink: requirements
17 for afterdepolarizations to propagate in tissue. *Biophys J.* 2010 Sep 8;99(5):1408–15.
- 18 31. Liu MB, de Lange E, Garfinkel A, Weiss JN, Qu Z. Delayed afterdepolarizations generate
19 both triggers and a vulnerable substrate promoting reentry in cardiac tissue. *Heart Rhythm*
20 *Off J Heart Rhythm Soc.* 2015 Oct;12(10):2115–24.
- 21 32. Colman MA, Parra-Rojas C, Perez-Alday EA. From microscopic calcium sparks to the
22 ECG: Model reduction approaches for multi-scale cardiac simulation. In: 2015
23 Computing in Cardiology Conference (CinC). 2015. p. 325–8.
- 24
25
26
27

1 **Figures**



2
3
4
5
6
7
8
9
10
11
12

Figure 1: Intracellular Ca^{2+} handling phenomena. A – Schematic of the cardiac Ca^{2+} handling system (left) illustrating the phases of calcium-induced-calcium-release during electrical excitation, with the relationship between the AP and Ca^{2+} transient (right). The primary fluxes are illustrated with the coloured ovals and directional arrows, and the phases of CICR are labelled: 1) Ca^{2+} influx through the LTCCs during excitation; 2) Ca^{2+} release from the SR through the RyRs; 3) diffusion into the bulk intracellular space; 4) binding with the contractile proteins; 5) mechanical relaxation releases Ca^{2+} back into the bulk space; 6) refilling of the SR through SERCA and Ca^{2+} -efflux through NCX. B – illustration of the mechanisms

1 of spontaneous excitation. The left panels show snapshots of calcium dynamics in the
2 schematic (upper) and using simulated data (lower). In the upper panels, the green regions
3 indicate high Ca^{2+} concentration and dyads undergoing Ca^{2+} release are circled in red dotted
4 lines. Illustrated are: 1) spontaneous Ca^{2+} spark; 2) propagation in the transverse direction
5 triggering more sparks; 3) propagation in the longitudinal direction, activating dyads on
6 neighbouring T-tubules. The right panel shows examples of the Ca^{2+} concentration, I_{NCX}
7 waveform and membrane potential associated with a stimulated excitation followed by a
8 spontaneous Ca^{2+} release event, illustrating a case in which the DAD both does and does not
9 manifest as a full triggered AP; the dotted line represents zero in y.
10

1
2
3
4
5
6
7
8
9
10
11
12
13
14
15
16

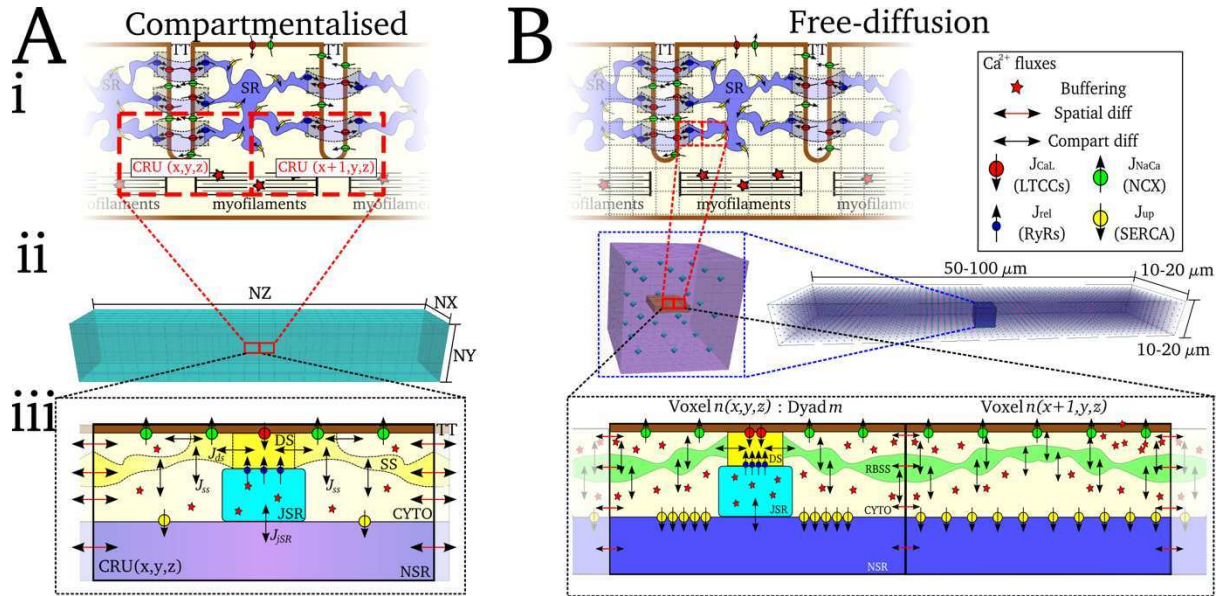
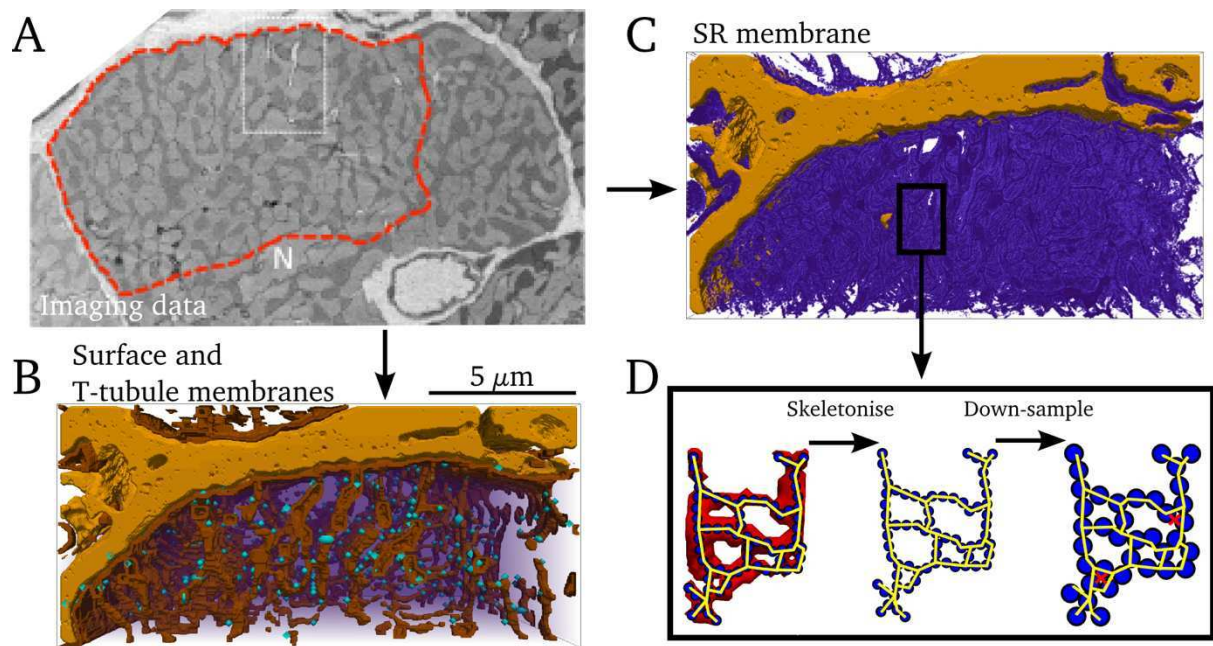
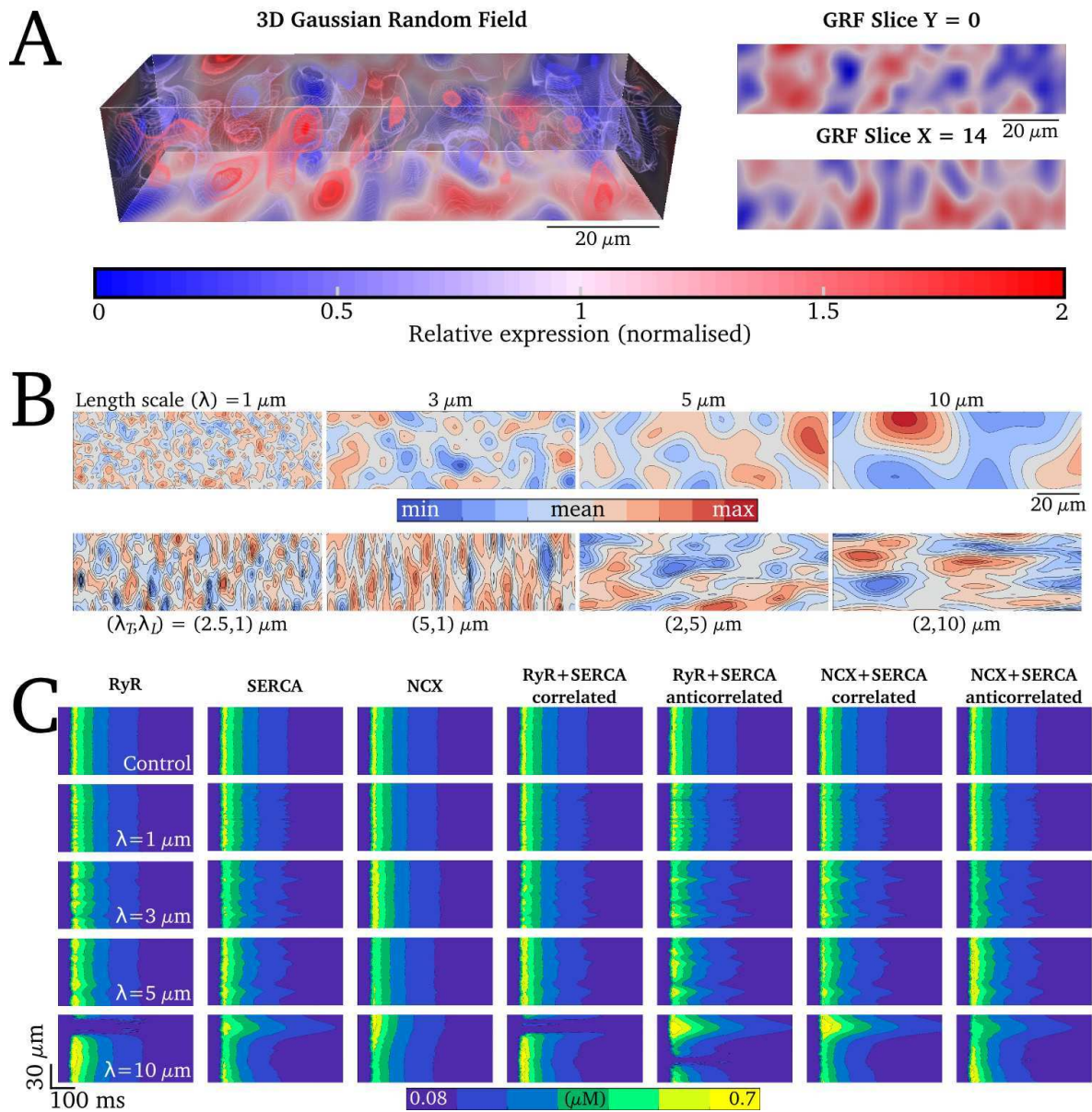


Figure 2: Schematics of the two different approaches for spatial cell modelling. A – the compartmentalised model involves coarse-graining the volumes associated with each dyad into a calcium-release-unit (i; CRU), which are arranged in a regular grid to form the cell (ii). The compartments of each CRU and the relevant fluxes and inter-compartment transfer are illustrated in (iii). Labelled are the dyadic cleft space (DS), sub-space (SS), bulk cytosolic space (CYTO), network and junctional SR spaces (NSR, JSR), and a T-tubule (TT). B – the free-diffusion model involves discretising the intracellular space as a free-diffusion volume (i), with voxels which both do and do not contain dyads; dyads are regularly distributed throughout the volume of the intracellular space (ii). The structure of each voxel is almost identical to that of a CRU (iii), with the exception of the presence or absence of dyads, TTs or the SR (according to the maps).



1
2 **Figure 3: Processing structural data for direct image-based modelling.** A – Example of a
3 slice of electron-microscopy images of cardiac sub-cellular structure from which simulation
4 geometries can be produced (data from [24] and image from [12]). B – Reconstruction of the
5 surface sarcolemma (light brown), T-tubules (dark brown) and dyad locations (blue dots)
6 within the intracellular space (purple volume). C – Reconstruction of the SR in 3D (purple)
7 and method for down-sampling (D).

1



2

3

4

5

6

7

8

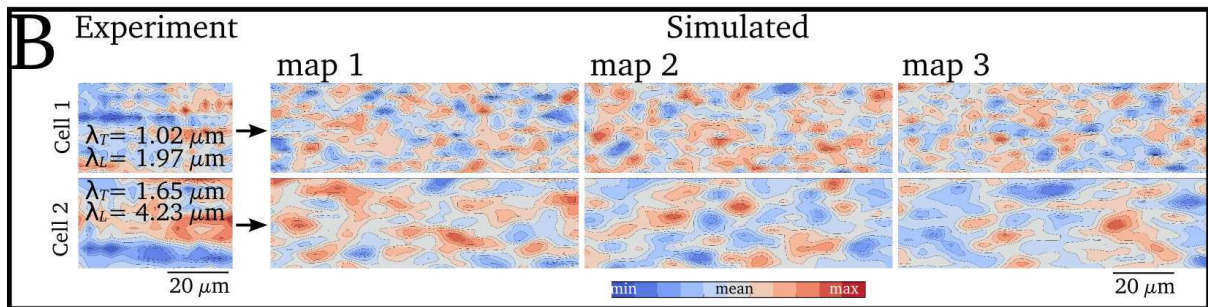
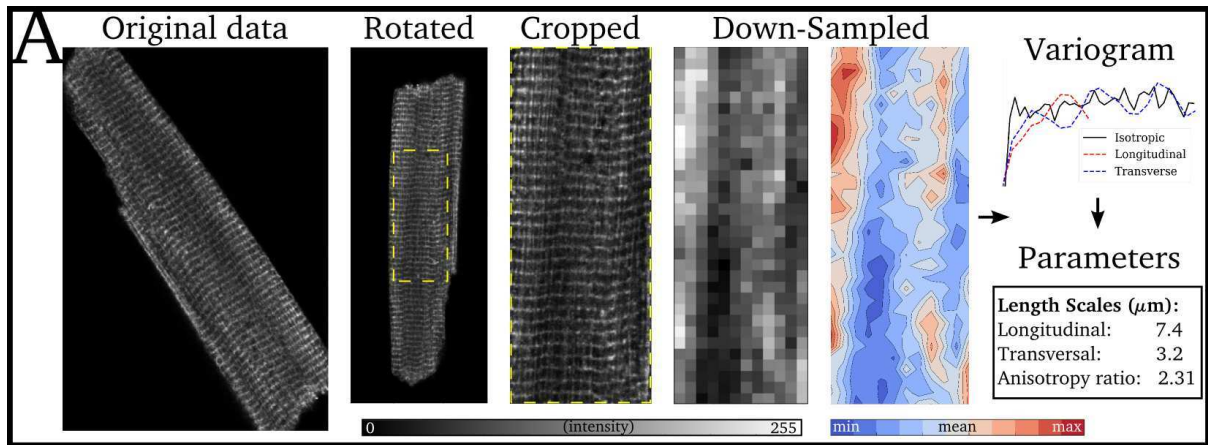
9

10

11

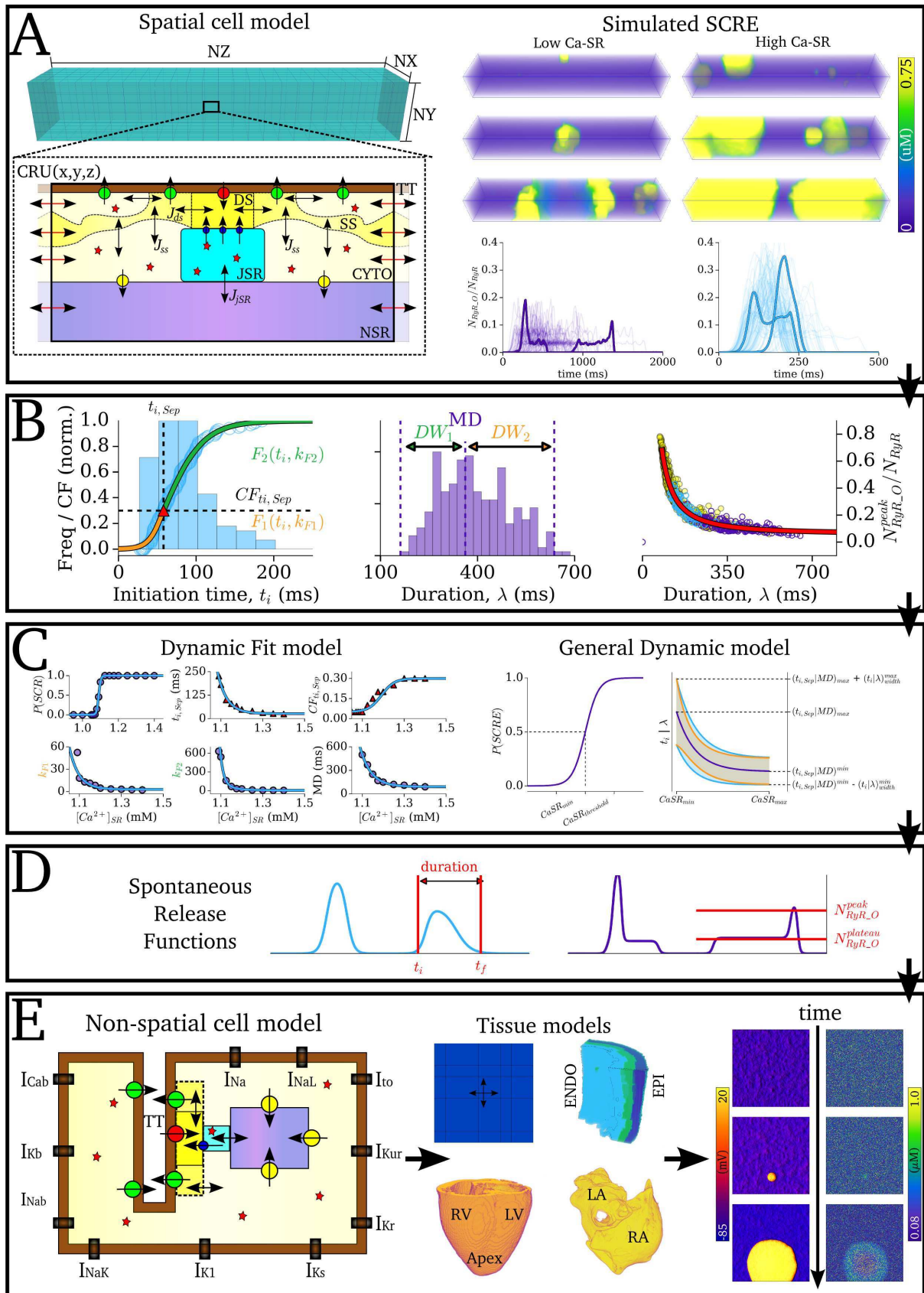
12

Figure 4: Illustration of using spatial random fields to model sub-cellular channel expression heterogeneity. A – Example of a 3D GRF map, visualised using a contour plot applied to 2D slices of the back surfaces, and semi-transparent contours throughout the volume; two individual 2D slices are also shown for clarity. B – Example slices showing isotropic (upper) and anisotropic (lower) GRF maps produced at different length scales and anisotropy ratios. C – Examples of the influence of sub-cellular heterogeneity in RyR, SERCA and/or NCX emerging from GRF maps with different length-scales. The plot visualises a linescan of Ca^{2+} concentration along the longitudinal axis of the cell (y-axis) in time (x-axis).



1
2
3
4
5
6
7
8

Figure 5: Image-based modelling using the compartmentalised models. A – Illustration of the processing required to extract length scales from cellular imaging data (in this example of SERCA expression). B – Examples of 2D slices from three independently produced GRF maps based on the parameters extracted from two different cells.



1
2
3
4
5

Figure 6: The computational framework for multi-scale simulation of spontaneous calcium release. A - 3D, microscopic Ca^{2+} handling model (left), illustrating the 3D grid of calcium release units (CRUs; upper panel) and the compartments and Ca^{2+} fluxes within a single CRU (lower panel). Labelled are the dyadic cleft space (DS), sub-space (SS), bulk

1 cytosolic space (CYTO), network and junctional SR spaces (NSR, JSR), and a T-tubule (TT);
2 simulated SCORE (right) showing three snapshots of Ca^{2+} waves at low (left) and high (right)
3 SR- Ca^{2+} ; lower panels are overlays of 100 simulations at each SR- Ca^{2+} . B – Statistics of SCORE,
4 showing the distributions associated with initiation time (left), duration (middle) and peak RyR
5 (right). Examples of two functions – and their relevant parameters – to fit the cumulative
6 frequency of initiation time are shown. C – Defining the distribution parameters based on SR-
7 Ca^{2+} , illustrating the Dynamic Fit model (left) and General Dynamic model (right). D –
8 Illustration of the analytical spontaneous release functions, defined by the parameters randomly
9 sampled from the initiation time and duration distributions. Those illustrated correspond to the
10 highlighted waveforms in A. E – Schematic of the non-spatial cell model (left), illustration of
11 the tissue models (middle), and example simulation of a SCORE mediated focal excitation
12 (right).